https://doi.org/10.1038/s44386-026-00076-z

RUNX2 inhibitor CADD522 improves bone microarchitecture and lipid metabolism in post-menopausal bone loss

Adel Ersek[1], Myoung Sook Kim[2], Caterina Suelzu[1], Isabelle Piec[3], Aerielle Matsangos[2], Elmar Nurmemmedov[4], Emma C. Bull[1], Tabitha Bartlett[1], Rachel Dunn[1], James R. Dick[5], Rena Lapidus[2], Danielle M. Copeman[1], Jonathan C. Y. Tang[1], Paul G. Crichton[1], Matthew G. Pontifex[1], William D. Fraser[1], Nicole J. Horwood[1], Antonino Passaniti[2,6] ✉ & Darrell Green[1,6] ✉

Osteoporosis is a leading cause of age-related morbidity, yet existing antiresorptive and anabolic therapies remain limited by safety concerns, contraindications and poor long-term adherence. CADD522 is a small molecule inhibitor of the RUNX2 transcription factor currently under development for cancer therapy. Here, we investigated whether RUNX2 inhibition could protect against post-menopausal bone loss. In an ovariectomy-induced mouse model, CADD522 (25 mg/kg, three times weekly for eight weeks) enhanced bone formation, preserved trabecular microarchitecture and reduced marrow and peripheral adiposity. Cross-species pharmacokinetic and toxicological studies demonstrated oral bioavailability, favourable short-term tolerability and target engagement despite rapid systemic clearance, while cellular thermal shift assays confirmed direct engagement of RUNX2. Together, these findings identify RUNX2 inhibition as a therapeutic strategy that simultaneously improves skeletal integrity and metabolic homeostasis, supporting further development of CADD522 for osteoporosis and other RUNX2-driven diseases.

Osteoporosis is a metabolic bone disorder characterised by low bone mass, structural deterioration and increased fracture risk[1]. Osteoporosis affects one in three women and one in five men aged over 50 worldwide[2] with ~20% one-year mortality following hip fracture and five-year survival rates comparable to thyroid and breast cancer[3]. Osteoporosis economic and healthcare burden is substantial, costing more than $20 billion annually in the US[4]. Osteoporotic fractures are the leading cause of hospitalisation in women aged >45 years in the UK[5].

Current therapies are limited. Antiresorptives such as bisphosphonates and denosumab reduce fracture risk[2,6,7] but long-term use carries risks of atypical femoral fractures and osteonecrosis of the jaw[8]. Anabolic agents, including parathyroid hormone (PTH) derivatives and analogues, namely teriparatide and abaloparatide, are effective[9] but require daily injection. Romosozumab offers monthly dosing but has cardiovascular safety concerns[10]. Hormone replacement therapy also reduces fracture risk[11,12] but its association with breast, ovarian and uterine cancer risk limits patient uptake[13]. Thus, new treatments with few side effects and broader applicability remain a clinical priority.

We recently evaluated the small molecule RUNX2 antagonist CADD522 in several preclinical cancer models[14–17]. RUNX2 is critical for in utero skeletogenesis[18] and cancer metastasis[19–22]. Unexpectedly, CADD522 reduced cancer-induced bone disease, suggesting potential utility in osteoporosis[14]. We therefore tested CADD522 in a post-menopausal bone loss model, confirming significant therapeutic benefit. Supporting in vivo pharmacokinetic (PK), toxicology and in vitro drug property studies demonstrated tolerability and RUNX2 engagement, providing a foundation for future human absorption, distribution, metabolism, and excretion (ADME) optimisation.

Results

CADD522 improves bone microarchitecture in wild-type control and ovariectomised (OVX) mice

Microcomputed tomography (μ-CT) analysis of tibias showed that the CADD522 regimen (Fig. 1a) increased bone volume in wild-type and OVX mice compared to empty vehicle controls (Fig. 1b, c). Bone surface density was unchanged in control mice but increased in OVX-CADD522 (Fig. 1d).

[1]Norwich Medical School, University of East Anglia, Norwich Research Park, Norwich, UK. [2]Pathology, Biochemistry, Molecular Biology, Greenebaum Comprehensive Cancer Center, School of Medicine, University of Maryland, Baltimore, Maryland, United States, The Veteran's Health Administration Research and Development Service, Baltimore, MD, USA. [3]School of Biological Sciences, University of East Anglia, Norwich Research Park, Norwich, UK. [4]The Scintillon Research Institute, San Diego, CA, USA. [5]Institute of Aquaculture, University of Stirling, Stirling, UK. [6]These authors contributed equally: Antonino Passaniti, Darrell Green. ✉e-mail: tpassaniti3@gmail.com; d.green@uea.ac.uk

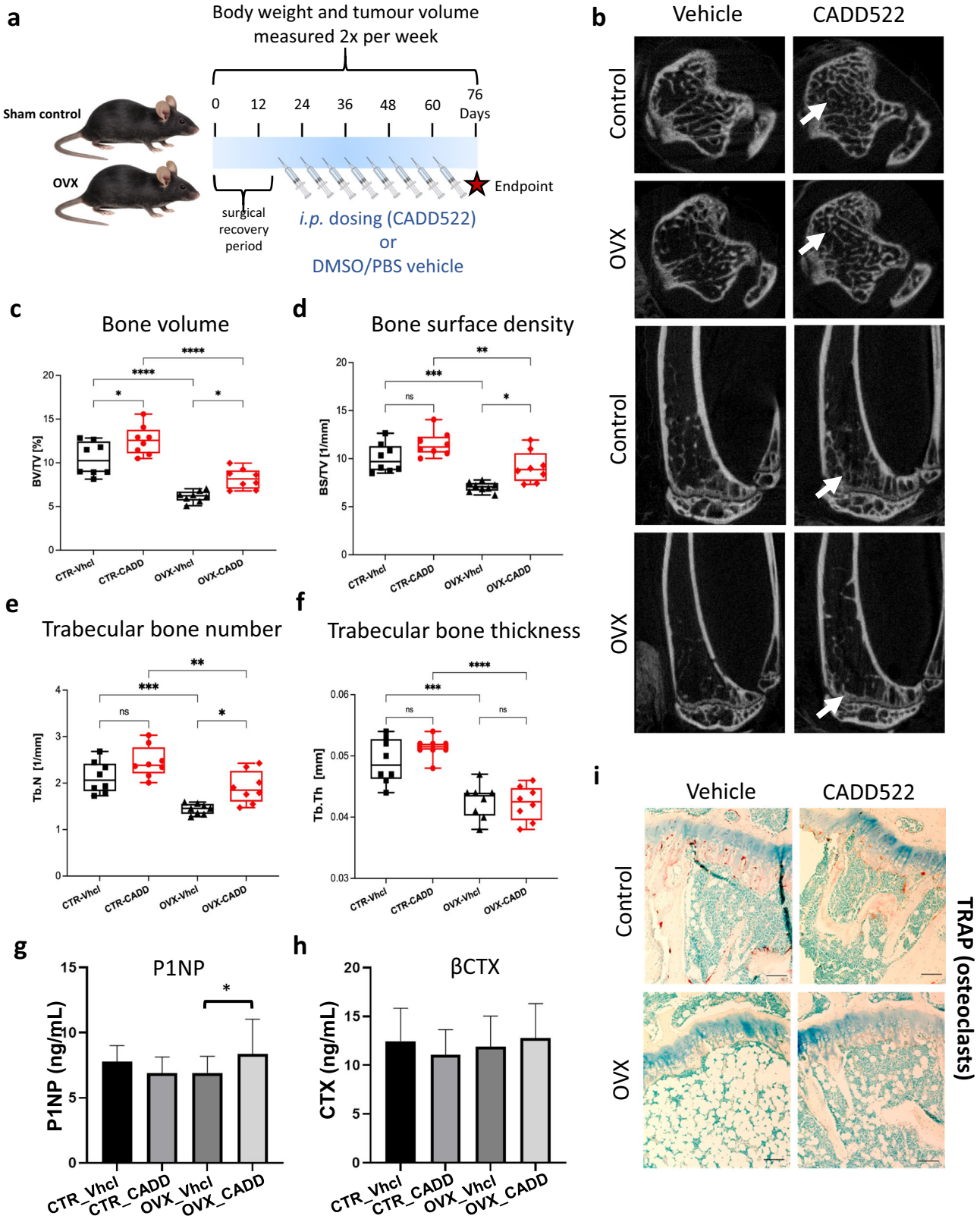

Fig. 1 | CADD522 bone effects in 16 sham and 16 OVX C57BL/6 J female mice. Both experimental models received either vehicle ($n = 8$) or CADD522 (25 mg/kg three times weekly for 8 weeks; $n = 8$). **a** Schematic showing the CADD522 treatment schedule. **b** Microcomputed tomography (μ-CT) reconstructed images of tibiae. White arrows indicate enhanced bone volume/thickness. **c** Bone volume. **d** Bone surface density. **e** Trabecular number. **f** Trabecular thickness. **g** PINP plasma levels. **h** βCTX plasma levels. **i** Representative TRAP staining of the tibial bone marrow below the growth plate in control and OVX mice. Scale bars = 100 μM.

Trabecular number was preserved in OVX-CADD522, comparable to control mice (Fig. 1e), while trabecular thickness was unaffected (Fig. 1f). Circulating procollagen type 1 N-propeptide (P1NP), a collagen formation biomarker, was elevated in OVX-CADD522 (Fig. 1g). C-terminal telopeptide of type 1 collagen (βCTX), a bone resorption marker, remained unchanged (Fig. 1h).

Tartrate-resistant acid phosphatase (TRAP) staining was used to assess osteoclast number and distribution along trabecular bone surfaces. Control-vehicle mice exhibited a moderate number of TRAP-positive osteoclasts lining trabeculae in a discontinuous pattern (Fig. 1i). Control-CADD522 mice had reduced osteoclast number with sparse and localised TRAP-positive cells (Fig. 1i). In OVX-vehicle, TRAP-positive cells were rare, with minimal osteoclast attachment and increased marrow adiposity (Fig. 1i). In contrast, OVX-CADD522 showed a marked increase in TRAP-positive multinucleated osteoclasts distributed more continuously along trabecular surfaces (Fig. 1i).

CADD522 reduces adipose tissue and improves lipid metabolism in OVX mice

CADD522 reduced body weight in OVX but not control mice (Fig. 2a) independent of appetite (Supplementary Data 1). Bilateral inguinal fat pad weight was lower in OVX-CADD522 (Fig. 2b, c). Gross pathology revealed reduced white adipose tissue without obvious brown adipose tissue development (Fig. 2d). Histological analyses of the tibias showed reduced adipocyte deposits in the bone marrow of OVX-CADD522 (Fig. 2e). Consistently, CADD522 ligand interaction did not activate Uncoupling protein 1 (UCP1) from brown fat (Supplementary Fig. S1a, b). To investigate CADD522 effects on lipid metabolism, we profiled total and phospholipid-associated fatty acids in the lipid-rich brains of three mice from each experimental group (Fig. 2f, g). CADD522 induced widespread remodelling of the fatty acid landscape, with the most pronounced effects observed in the phospholipid fraction. Notably, treatment shifted phospholipid profiles towards those observed in non-OVX control animals, suggesting a partial restoration of menopause-associated lipid alterations (Fig. 2f). In the phospholipid fraction, the most pronounced CADD522 effects were in the long-chain saturated fatty acids (Fig. 2g). Treatment significantly reduced the abundance of arachidic acid, docosanoic acid and lignoceric acid in OVX mice, reversing the accumulation observed in vehicle-treated animals (Fig. 2f, g). Similarly, CADD522 reshaped the monounsaturated fatty acid profile, increasing palmitoleic acid and vaccenic acid levels while normalising elevated erucic acid and nervonic acid concentrations towards those observed in control animals (Fig. 2g).

In contrast, CADD522 produced relatively modest effects on n-3 polyunsaturated fatty acids (Fig. 2f, g). Neither docosahexaenoic acid (DHA) nor total n-3 PUFA abundance was significantly altered by treatment, indicating that the metabolic effects of CADD522 were preferentially directed towards saturated and monounsaturated lipid pathways (Fig. 2g).

CADD522 pharmacokinetics (PK), tolerability and comparative hepatic metabolism

Pharmacokinetic and tolerability properties were assessed in mice, rats and dogs following intraperitoneal (IP), intravenous (IV) and oral (PO) administration (Fig. 3a). In CD-1 mice, high-dose oral CADD522 (40 mg/kg, single dose) reached peak plasma concentration (C_{max} 60 mg/mL, ~184 μM) in 15 min and had a half-life of ~1 h (Fig. 3b). Eight-day, high-dose oral administration (40 mg/kg, BID) showed minimal toxicity with mild leukopenia (Fig. 3c) and mild increases in liver alkaline phosphatase (ALP) and cholesterol (Fig. 3d). In rats, IV dosing resulted in low exposure (mean $AUC_{(0\text{-}inf)}$ 0.376 h*μmol/L) and rapid systemic elimination with a short half-life (t½ 1.01 h; Fig. 4a, b; Table 1), whereas oral dosing increased exposure ($AUC_{(0\text{-}inf)}$ 0.988 h*μmol/L) and prolonged the terminal phase (t½ 3.95 h), with low inter-animal variability (Fig. 4c-f; Table 1). In dogs, IV administration yielded similarly low exposure ($AUC_{(0\text{-}inf)}$ 0.188 h*μmol/L) and more rapid clearance (t½ 20 min; Fig. 4g, h; Table 2), while oral dosing increased exposure ($AUC_{(0\text{-}inf)}$ 0.639 h*μmol/L), extended the half-life (t½ 39 min; Fig. 4i-l; Table 2) and resulted in moderate bioavailability (F = 67.5%; Table 2).

In vitro metabolic stability of CADD522 was then evaluated in mouse, rat, dog, minipig and human hepatic microsomes. Cytochrome P450 (CYP450) monooxygenase processing using 10 μM [^{14}C]-testosterone as the positive control (Fig. 4m) showed species differences in intrinsic clearance, with rapid metabolism observed in rodent microsomes and greater stability in higher species (Fig. 4n). In mouse microsomes, CADD522 was rapidly depleted with only half the parent compound remaining by 30 min (Fig. 4n). In contrast, degradation was slower in higher species' microsomes (Fig. 4n), indicating moderate metabolic stability. Notably, CADD522 was most stable in human microsomes with a substantial fraction of parent compound remaining over the duration of the assay (Fig. 4n), suggesting comparatively low intrinsic clearance.

CADD522 engages RUNX2 and structure-function analogues

Cellular thermal shift assay (CETSA) confirmed dose-dependent RUNX2 engagement (EC50 116 nM) with CADD522 stabilising RUNX2 at 55 °C (Fig. 5a-d; Supplementary Fig. S1c, d). Structural analogue testing revealed that a bulky weak electron-withdrawing group at carbon-4 was essential for drug activity (Fig. 5e-h). Functional assays using an in vitro spheroid model showed that CADD522 and active analogues inhibited growth of RUNX2-expressing TWIST2+ cells but not RUNX2-negative PHMLEB cells (Fig. 6a-c).

Discussion

Osteoporosis remains a major cause of age-related disability despite the availability of effective antiresorptive and anabolic therapies. Although current treatments reduce fracture risk, long-term adherence is limited by adverse effects, contraindications and the need for repeated administration by a trained healthcare professional, highlighting the continued need for therapeutics with alternative mechanisms of action. In this study, we demonstrate that pharmacological inhibition of RUNX2 using the small molecule CADD522[14–16] protects against ovariectomy-induced bone loss while simultaneously reducing adiposity and selectively remodelling systemic lipid metabolism. Together with evidence of direct target engagement, oral bioavailability and favourable early tolerability, these findings identify RUNX2 inhibition as a therapeutic strategy with potential applications extending beyond its original development as an anticancer agent.

RUNX2 is widely recognised as the master regulator of osteoblast differentiation and skeletal development[18,23–28], making the observation that pharmacological RUNX2 inhibition improves bone architecture initially counterintuitive. However, developmental functions of transcription factors frequently differ from their roles in mature tissues[29–31]. Our findings support the concept that RUNX2 contributes to pathological remodelling in the adult skeleton, where its inhibition enhances bone formation and preserves trabecular architecture following oestrogen deficiency. Rather than suppressing bone turnover globally, CADD522 increased circulating P1NP without altering βCTX, consistent with a net anabolic response. Histological changes in osteoclast distribution further suggest that RUNX2 inhibition modifies remodelling dynamics rather than simply inhibiting osteoclastogenesis. Together, these observations indicate that preservation of skeletal integrity is achieved through restoration of balanced bone remodelling rather than conventional antiresorptive activity.

The concept of combining osteoanabolic and anti-remodelling activities within a single therapeutic platform has gained increasing attention in bone regenerative medicine. Hydroxyapatite-based multifunctional nanocomposites co-delivering bisphosphonates together with osteogenic ions, including zinc [need reference PMID: 27040198] or strontium [need reference PMID: 27987763], have previously demonstrated synergistic enhancement of bone regeneration while simultaneously suppressing pathological bone resorption. Similarly, zoledronate-loaded hydroxyapatite nanoparticles have improved bone remodelling through concurrent osteoconductive and antiresorptive effects [need reference PMID: 25444840]. These earlier studies illustrate the therapeutic value of

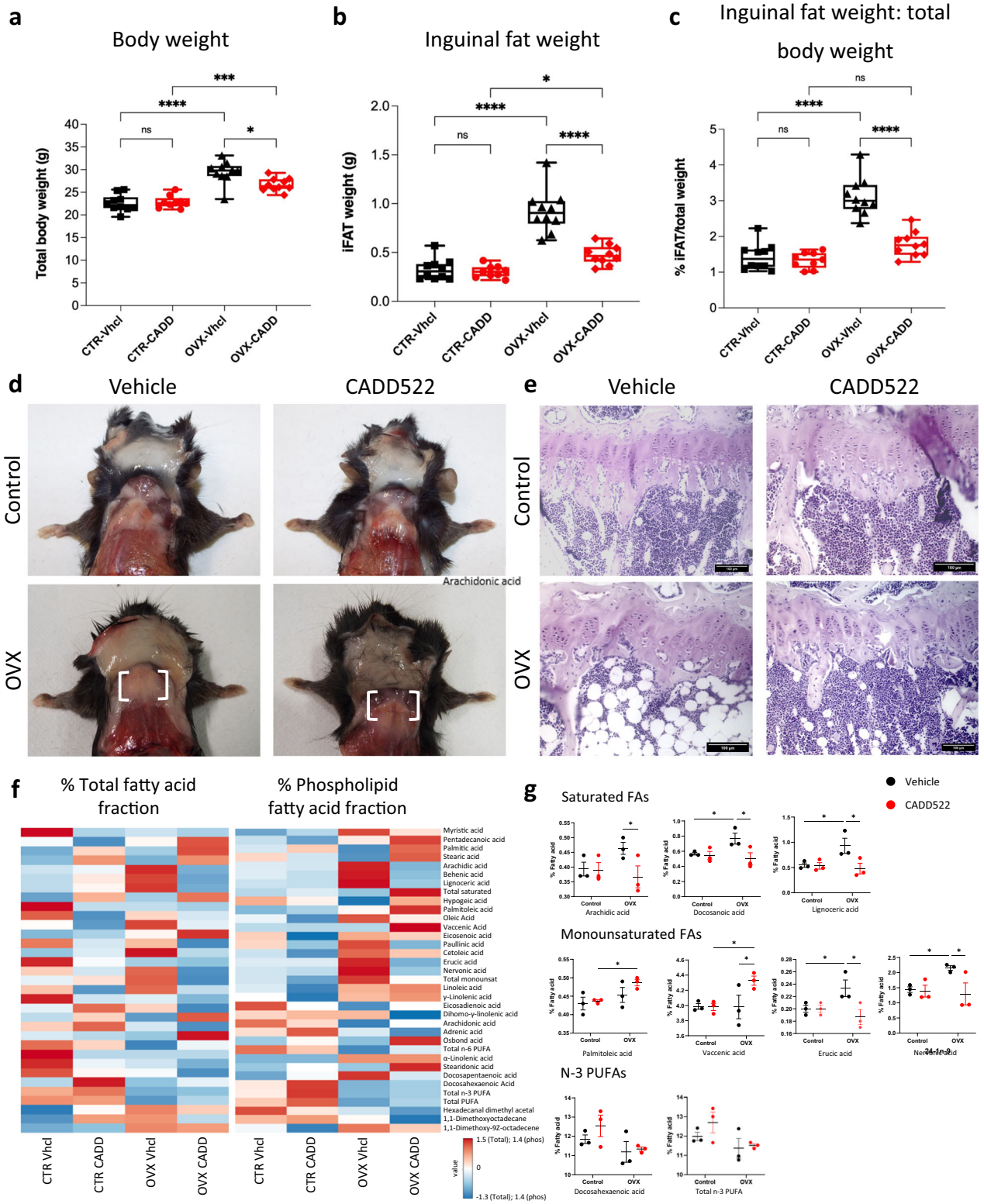

Fig. 2 | CADD522 adiposity effects in the same 16 sham and 16 OVX C57BL/6 J female mice. Both experimental models received either vehicle ($n = 8$) or CADD522 (25 mg/kg three times weekly for 8 weeks; $n = 8$). **a** Body weight. **b** Inguinal fat weight. **c** % inguinal fat/total body weight. **d** Representative suprascapula white adipose tissue gross pathology (white brackets). **e** Representative H&E staining of the tibial bone marrow below the growth plate. Scale bar=100 µM. **f** Global lipidomic analysis in $n = 3$ brains from all experimental groups. Left panel = % total fatty acid fraction. Right panel = % phospholipid fraction. **g** statistical significance in saturated fatty acids, monounsaturated fatty acids, and *n*-3 polyunsaturated fatty acids.

integrating complementary biological activities within a single intervention rather than relying on agents that exclusively stimulate bone formation or inhibit resorption. Contrastingly to these biomaterial-based approaches, CADD522 achieves biological activity through pharmacological inhibition of the RUNX2 transcription factor, simultaneously preserving trabecular architecture, promoting bone formation and reducing adiposity and metabolic dysfunction. Although mechanistically distinct, these findings place CADD522 within the broader landscape of multifunctional bone

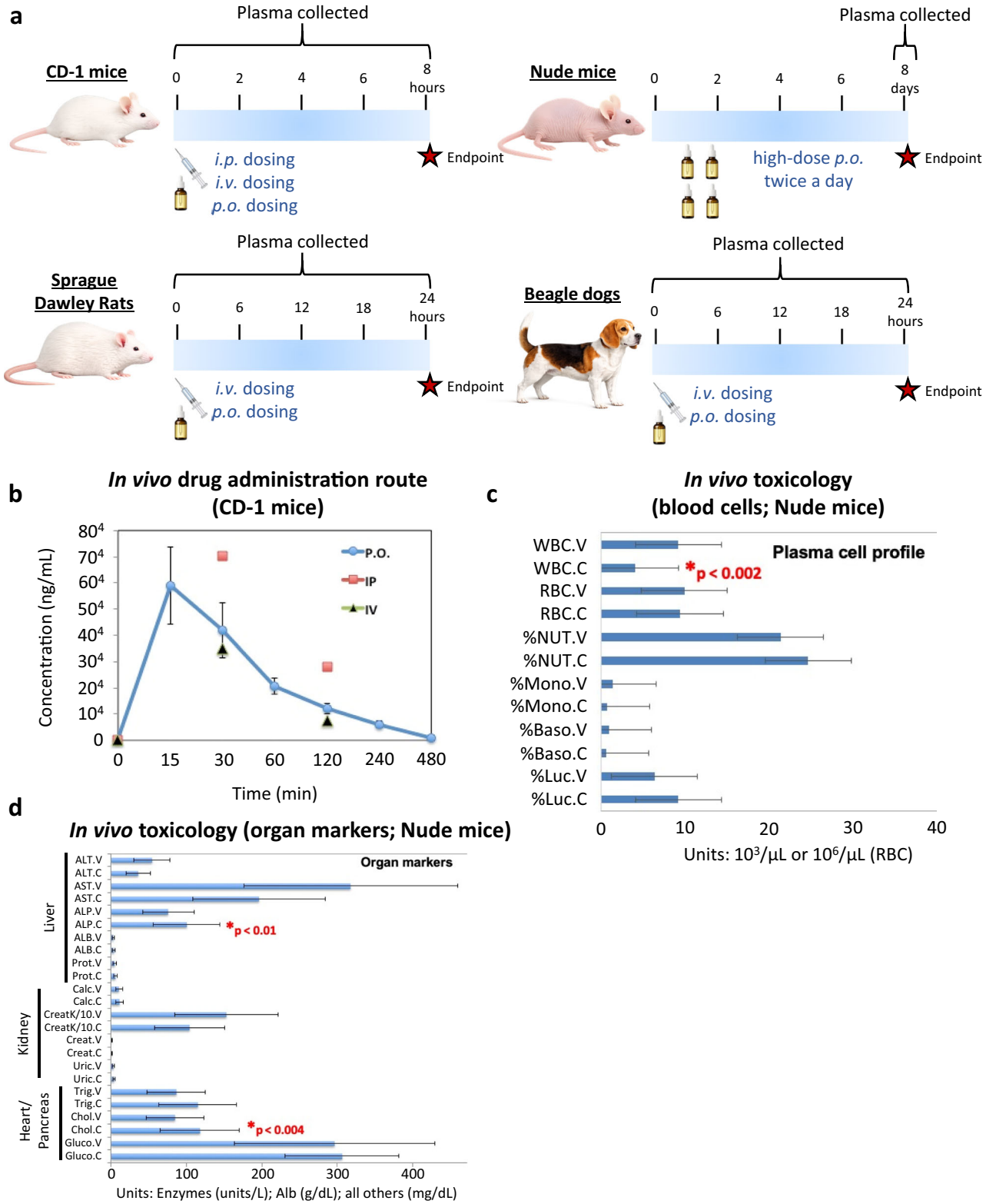

Fig. 3 | Pharmacokinetics and tolerability in CD-1 ($n = 6$) and Nude ($n = 5$) mice. **a** Schematic showing CADD522 tolerability schedules and animals. **b** Plasma levels following single 40 mg/kg IP, IV or PO dosing (CD-1 mice). **c** Blood cell profiles after 8 days of twice-daily 40 mg/kg PO dosing (nude mice). **d** Organ toxicity markers (ALT, AST, ALP, ALB, Prot, Calc, CreatK, Uric, Trig, Chol, Gluc). Significant differences shown (p-values). WBC white blood cells/leukocytes, RBC red blood cells, NUT neutrophils, Mono monocytes, Baso basophils, Luc large unstained cells, which correlate with markers of immune activation and helper T cell (CD4) counts, ALT alanine transaminase, AST aspartate transaminase, ALP alkaline phosphatase, ALB albumin, Prot total protein, Calc calcium, CreatK creatinine kinase, Uric uric acid; Trig, triglycerides; Chol, cholesterol, Gluco glucose. Standard units on the x-axis are specific for each enzyme/metabolite.

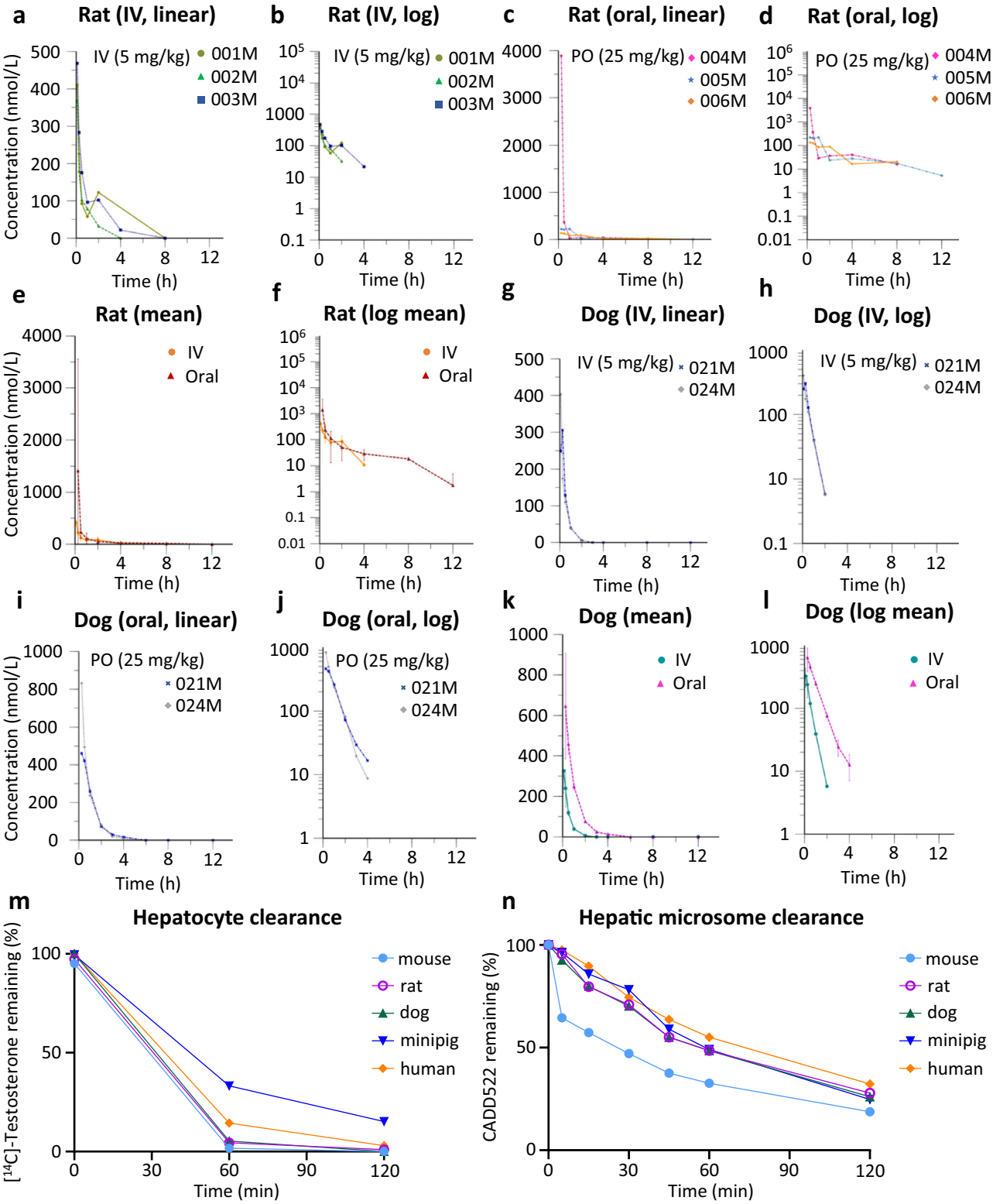

Fig. 4 | Pharmacokinetics after single dose in rats ($n = 6$) and dogs ($n = 2$). **a**–**f** Plasma concentrations in Sprague Dawley rats (IV 5 mg/kg, PO 25 mg/kg). **g**–**l** Plasma concentrations in Beagle dogs (IV 5 mg/kg, PO 25 mg/kg). Linear and log plots shown for individual and mean values. **m** in vitro hepatic clearance of 10 μM [^{14}C]-testosterone and **n** 1 μM CADD522 in mice, rats, dogs, minipigs and humans. Experiments were performed in duplicate.

therapeutics and support the concept that coordinated modulation of skeletal and metabolic pathways may provide greater therapeutic benefit than those targeting bone remodelling alone.

A remarkable finding was that the skeletal improvements occurred alongside reduced peripheral and marrow adiposity and selective remodelling of lipid metabolism. Oestrogen deficiency is accompanied by profound metabolic changes that extend beyond bone, including increased adiposity and altered lipid handling. CADD522 consistently reduced body weight, inguinal fat mass and marrow adipocyte accumulation without evidence of UCP1-mediated thermogenesis, suggesting that these effects are

Table 1 | Pharmacokinetic parameters of CADD522 following IV (5 mg/kg) and PO (25 mg/kg) administration to 6 male Sprague Dawley rats

Route	Dose level (mg/kg)	Animal number	C_0 (nmol/L)	C_{max} (nmol/L)	T_{max} (h)	$AUC_{(0-t)}$ (umol/L)	$AUC_{(0-inf)}$ (umol/L)	$T_{1/2}$ (h)	V_z (L/kg)	CL (mL/min/kg)	F (%)
IV	5	001 M	551	410	0.0830	0.261	NR	NR	NR	NR	NA
		002 M	525	368	0.0830	0.219	0.260	0.880	74.7	981	NA
		003 M	602	469	0.0830	0.455	0.491	1.14	51.2	519	NA
		N	3.00	3.00	3.00	2.00	2.00	2.00	2.00	2.00	NA
		Mean	559	415	0.0830	0.312	0.376	1.01	70.0	750	NA
		SD	39.4	50.7	NA	126	NA	NA	NA	NA	NA
		CV%	7.04	12.2	NA	40.5	NA	NA	NA	NA	NA
PO	25	004 M	NA	3890	0.250	1.34	1.45	4.58	350[a]	882[a]	NA
		005 M	NA	222	1.00	0.501	0.526	3.32	699[a]	2430[a]	NA
		006 M	NA	135	0.250	NR	NR	NR	NR	NR	NA
		N	NA	3.00	3.00	2.00	2.00	2.00	2.00	2.00	NA
		Mean	NA	1420	0.250	0.921	0.988	3.95	525	1656	52.4
		SD	NA	2140	0.250-1.00	NA	NA	NA	NA	NA	NA
		CV%	NA	151	NA	NA	NA	NA	NA	NA	NA

C_0 initial concentration, C_{max} peak serum concentration, T_{max} time of C_{max}, $AUC_{(0-t)}$ area under curve to last quantifiable timepoint, $AUC_{(0-inf)}$ area to infinity, $T_{1/2}$ terminal half-life, V_z volume of distribution, *CL* clearance, *F* oral bioavailability, *NA* not applicable, *NR* not reported (AUC extrapolated >20%or r^2 <0.8).
[a]Oral Cl and Vz calculated using apparent values (Cl/F, Vz/F). F% based on mean AUCinf (IV vs PO) due to non-crossover design.

Table 2 | Pharmacokinetic parameters of CADD522 following IV (5 mg/kg) and PO (25 mg/kg) administration to 2 male Beagle dogs

Route	Dose Level (mg/kg)	Animal number	C_0 (nmol/L)	C_{max} (nmol/L)	T_{max} (h)	$AUC_{(0-t)}$ (umol/L)	$AUC_{(0-inf)}$ (umol/L)	$T_{1/2}$ (h)	Vz (L/kg)	CL (mL/min/kg)	F (%)
IV	5	021 M	NR	305	0.250	0.186	0.189	0.338	39.5	1350	NA
		024 M	611	403	0.0830	0.185	0.188	0.353	41.5	1360	NA
		N	1.00	2.00	2.00	2.00	2.00	2.00	2.00	2.00	NA
		Mean	NA	354	0.167	0.186	0.188	0.346	40.5	1350	NA
PO	25	021 M	NA	461	0.250	0.579	0.596	0.725	135[a]	2140[a]	62.9
		024 M	NA	832	0.250	0.675	0.683	0.592	95.9[a]	1870[a]	72.0
		N	NA	2.00	2.00	2.00	2.00	2.00	2.00	2.00	2.00
		Mean	NA	646	0.250	0.627	0.639	0.659	115	2010	67.5

C_0 initial concentration, C_{max} peak serum concentration, T_{max} time of C_{max}, $AUC_{(0-t)}$ area under curve to last quantifiable timepoint, $AUC_{(0-inf)}$ area to infinity, $T_{1/2}$ terminal half-life, V_z volume of distribution, *CL* clearance, *F* oral bioavailability, *NA* not applicable, *NR* not reported (AUC extrapolated >20%or r^2 <0.8).
[a]Oral Cl and Vz calculated using apparent values (Cl/F, Vz/F). F% based on mean AUCinf (IV vs PO) due to non-crossover design.

unlikely to reflect increased energy expenditure through adipose browning. Lipidomic profiling in the lipid-rich brain further demonstrated preferential normalisation of long-chain saturated and monounsaturated fatty acids while largely preserving n-3 polyunsaturated fatty acids. Rather than inducing indiscriminate metabolic disruption, RUNX2 inhibition therefore appears to restore specific lipid pathways perturbed by menopause. These observations are notable because menopause is associated with widespread disruption of brain lipid homeostasis that has been linked to cognitive decline, and dietary n-3 polyunsaturated fatty acid supplementation has previously been shown to partially mitigate these changes[32,33]. Although the relationship between altered brain lipid composition and cognitive function was not examined in the present study, the selective remodelling of brain lipids following CADD522 treatment raises the possibility that RUNX2 inhibition may influence neurological adaptations to menopause in addition to preserving skeletal integrity. Future studies should determine whether these metabolic effects translate into improvements in cognition or other measures of brain health. More broadly, accumulating evidence implicates RUNX2 in transcriptional programmes regulating lipid metabolism across multiple tissues, supporting an emerging role for RUNX2 as a coordinator of skeletal and metabolic homeostasis.

Translation of transcription factor inhibitors has historically been constrained by uncertainties regarding target engagement and drug-like properties. Here, cellular thermal shift assays confirmed direct engagement of RUNX2 at sub-micromolar concentrations, while structure-activity relationship studies demonstrated that closely related analogues exhibited substantially reduced biological activity, supporting the specificity of CADD522. Cross-species pharmacokinetic studies further demonstrated oral absorption and favourable short-term tolerability despite relatively rapid systemic clearance. Importantly, hepatic microsome studies showed greater metabolic stability in human than rodent microsomes, suggesting that preclinical rodent pharmacokinetics may underestimate persistence in humans. Nevertheless, rapid in vivo clearance remains the principal developability challenge and provides a clear rationale for medicinal chemistry optimisation or formulation strategies to extend systemic exposure while maintaining target engagement.

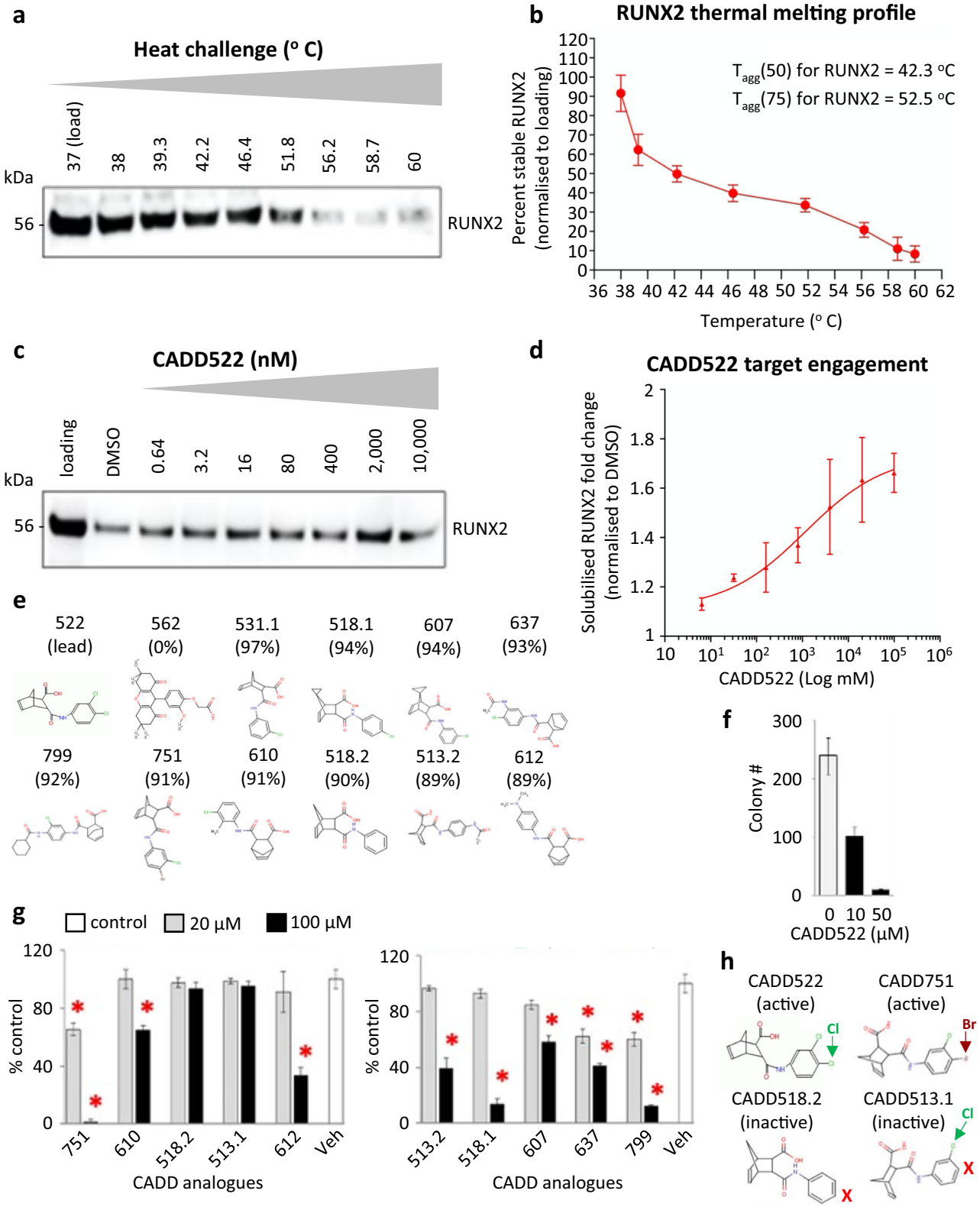

Fig. 5 | Cellular thermal shift assay (CETSA) and analogue activity. a–d RUNX2 CETSA: melting profile without drug (Tagg(75) = 52.5 °C) and dose-dependent CADD522 stabilisation (EC50 = 116 nM). **e** Lead analogues (>89% similarity) identified via hit2lead. **f**,–**g** CFA assays of CADD522 and analogues at varying doses. **h** Core structure and side group features relevant to activity.

Several limitations should be acknowledged. The efficacy studies were performed in a single ovariectomy model, and longer-term studies will be required to determine whether the skeletal benefits are maintained and ultimately reduce fracture risk. Lipidomic analyses were performed in a limited number of animals and therefore identify metabolic associations rather than establish causal mechanisms. Furthermore, although RUNX2 engagement was confirmed biophysically, the downstream transcriptional programmes responsible for the

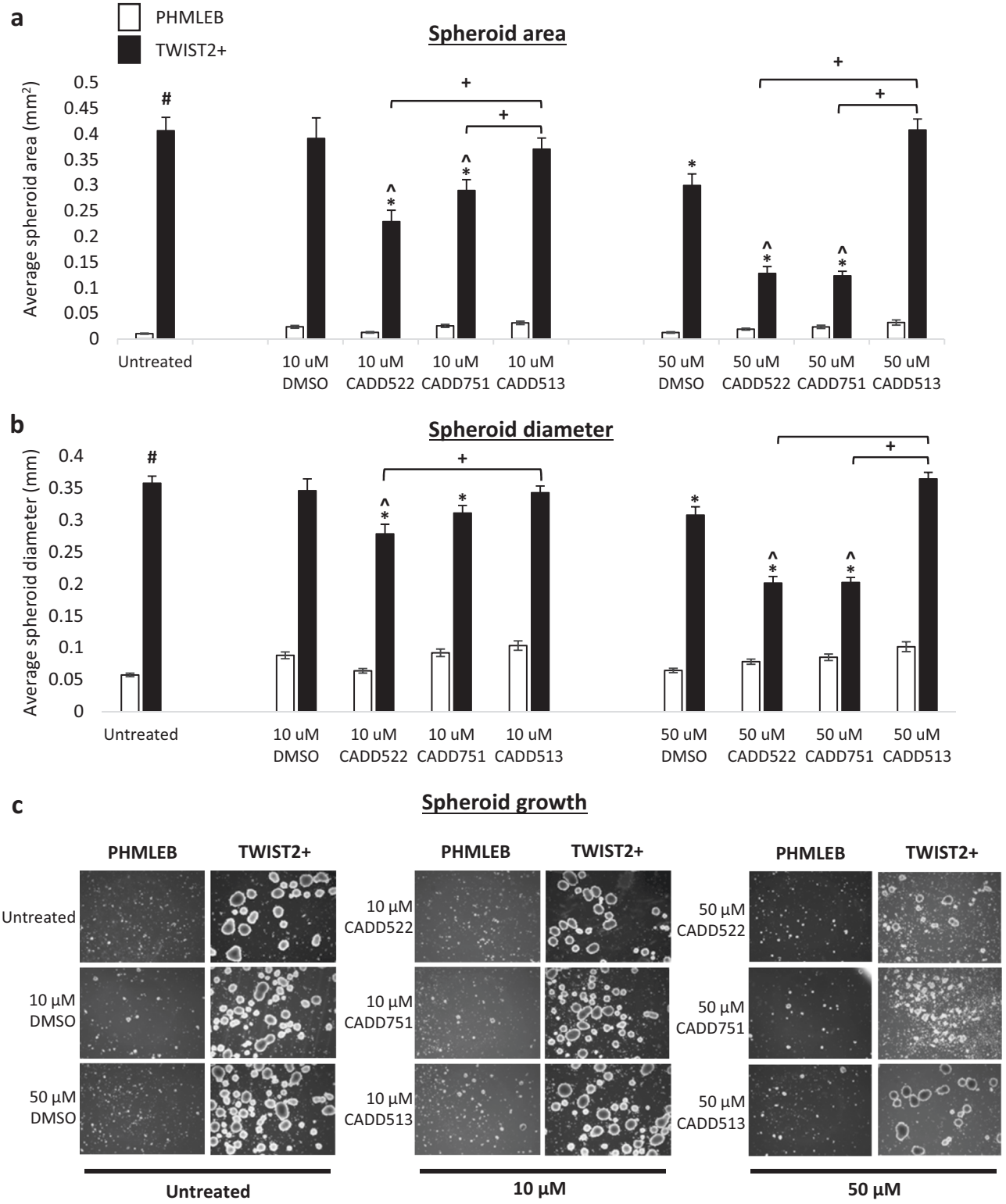

Fig. 6 | Structure-activity relationships and spheroid inhibition. a Spheroid area in PHMLEB and TWIST2+ cells treated with CADD522, CADD751 (active), or CADD513 (inactive). **b** Spheroid diameter under same conditions. **c** Representative 2X images after 1 week of treatment.

observed skeletal and metabolic phenotypes remain to be defined. Future studies should also investigate whether medicinal chemistry optimisation or advanced drug-delivery approaches, including sustained-release formulations or bone-targeted delivery systems, can enhance systemic exposure while preserving the favourable pharmacodynamic properties of CADD522.

In summary, our findings reveal an unexpected role for RUNX2 inhibition in protecting against post-menopausal bone loss while simultaneously improving systemic metabolic homeostasis. By integrating efficacy, lipidomics, pharmacokinetics, toxicology and direct target engagement, this study establishes a translational framework for further development of CADD522 and identifies RUNX2 as a

therapeutically tractable regulator of skeletal and metabolic adaptation in adulthood.

Methods

CADD522 preparation

CADD522 (Chembridge, 5221975; PubChem CID: 2834870) was >90% pure (HPLC) and stored at −20 °C. For in vivo use, CADD522 was dissolved in sterile DMSO/PBS/HPβCD (10%/70%/20% v/v/v), sonicated and filtered (0.22 μM PVDF).

In vivo efficacy studies

The study design was approved by the Animal Welfare and Ethical Review Body of the University of East Anglia Research Ethics Committee and performed under Project Licence PP5500397. All procedures complied with UK Home Office guidelines and the Animals (Scientific Procedures) Act 1986. Five-week-old female C57BL/6 J mice were randomised and underwent OVX or sham surgery under 2% isoflurane anaesthesia. After two-week recovery with free access to sunflower seeds for 5 days, sham ($n = 16$) and OVX ($n = 16$) mice received either 25 mg/kg CADD522 ($n = 8$) or DMSO/PBS vehicle ($n = 8$) via IP injection three times per week for eight weeks. Clinical signs were monitored. At study endpoint, animals were humanely killed using Schedule 1-regulated procedures: respiratory and cardiac arrest by increasing CO_2 concentration and cervical dislocation. Tibias were fixed in neutral buffered formalin then stored in 70% ethanol at 4 °C.

Inguinal fat analysis

Total body weight of the mice was measured three times per week. At study endpoint, the bilateral inguinal fat pads located adjacent to the genitals and running along the inner thighs were dissected by separation from the surrounding connective tissue using blunt dissection and fine forceps. Fat pads were weighed and stored en bloc at −80 °C.

Bone markers

At in vivo endpoint, 1 mL whole blood was collected into K_2EDTA tubes (Greiner Bio-One, 454024). Blood samples were centrifuged at 751 × *g* at 4 °C for 10 min before plasma was separated and stored at −80 °C. Plasma P1NP (IDS, IS-4000) and βCTX (IDS, IS-3000N) were measured by ELISA with intra-assay CV < 6% and LoQ of 0.33 and 4.5 ng/mL, respectively.

μ-CT

Tibias were scanned using the SkyScan 1174 (8.3 μm voxel resolution, 50 kV, 800 μA, 0.5 mm Al filter). Trabecular region-of-interest commenced below the growth plate and extended 208 slices (1.72 mm). Thresholding (80 density units) distinguished mineralised from non-mineralised tissue.

Suprascapula adipose tissue

Cadavers were inspected post-mortem for suprascapula white adipose tissue. Fat pads were photographed with a FinePix S9400W (Fujifilm).

Histology

Bones were decalcified in 14% EDTA over 10 days, paraffin-embedded and sectioned (5 μm) onto glass slides. Slides were dewaxed, rehydrated and stained with either haematoxylin and eosin (H&E) or TRAP stain (TRAP solution and then counterstained with 0.2% methyl green), dehydrated and mounted in DPX.

UCP1 assays

Thermostability of purified ovine UCP1 was assessed by CPM dye-based fluorescence melt analysis[34,35]. Liposome reconstitution with SPQ probe was used to assess proton flux[36–40].

Fatty acid profiling

Total lipids from whole brain samples ($n = 3$/group) were extracted as previously described[41]. Non-lipid impurities were removed by washing with 0.88% (w/v) potassium chloride. Lipid weight was determined gravimetrically after solvent evaporation and overnight desiccation under vacuum. Fatty acid methyl esters (FAMEs) were prepared by acid-catalysed transesterification of total lipids[42]. Extraction and purification of FAMEs was performed as previously described[43] before being separated by gas-liquid chromatography using a Trace GC 2000 (Thermo Fisher Scientific) equipped with a fused silica capillary column (ZBWax, 60 m × 0.32 × 0.25 mm inner diameter; Danaher) with hydrogen as carrier gas and using on-column injection. Temperature gradient was 50–150 °C at 40 °C/min, then to 195 °C at 1.5 °C/min, and finally to 220 °C at 2 °C/min. Individual methyl esters were identified by comparison to known standards (Supelco 37-Fame Mix; MilliporeSigma) and by reference to previously published data[41]. Data were collected and processed using the Chromcard for Windows (v.2.00) computer package (Thermoquest). Fatty acid content per gram of tissue was calculated using heptadecanoic acid as internal standard.

In vivo toxicology

The study design was approved by the Institutional Animal Care and Use Committee at the University of Maryland. All procedures complied with The Animal Welfare Act. Female CD-1 ($n = 6$) and nude mice ($n = 5$) received a single IP, IV or PO 40 mg/kg dose or repeated PO dosing (40 mg/kg BID × 8 days). Plasma was collected at multiple timepoints and analysed by LC-MS/MS. At study endpoint, mice were humanely killed in accordance with the American Veterinary Medical Association Guidelines for the Euthanasia of Animals: respiratory and cardiac arrest by increasing CO_2 concentration and cervical dislocation.

In vivo PK

The study design was approved by the Animal Welfare and Ethical Review Body of Charles River Laboratories, Edinburgh, UK and performed under Project Licence PP9376768. All procedures complied with UK Home Office guidelines and the Animals (Scientific Procedures) Act 1986. Male Sprague Dawley rats ($n = 6$) received 5 mg/kg IV or 25 mg/kg PO CADD522. Male Beagle dogs ($n = 2$) received 5 mg/kg IV, and one-week later, received 25 mg/kg PO. Plasma was collected up to 24 h and analysed by LC-MS/MS. At study endpoint, rats were humanely killed using Schedule 1 procedures: respiratory and cardiac arrest by increasing CO_2 concentration and cervical dislocation. Dogs were adopted through a beagle rehoming scheme.

Hepatic microsome metabolism assay

1×10^6 primary hepatocytes and hepatic microsomes from CD-1 mice, Sprague Dawley rats, Beagle dogs, Göttingen minipigs and humans (Discovery Life Sciences) were plated into 12-well plates and incubated in duplicates in a shaking water bath set to 37 °C with 1 μM CADD522 or 10 μM [^{14}C]-testosterone (positive control), 1 mM nicotinamide adenine dinucleotide phosphate (NADPH) and incubation medium in a final volume of 1 mL. After 0, 5, 15, 30, 45, 60 and 120 min, 100 μL aliquots of the incubation supernatant were combined with an equal volume (100 μL) of ice-cold termination solvent. Experiments in heat-deactivated microsomes and blank samples (negative controls) were conducted in parallel. Terminated samples were transferred to a −20 °C freezer for 30 min then allowed to reach room temperature, vortex-mixed and particulate matter removed by centrifugation at 10,000 × *g* for 10 min. [^{14}C]-testosterone was detected by stable isotope dilution (SID)-LC-MS/MS[44]. CADD522 was detected by LC-MS/MS. In vitro intrinsic clearance (CL_{int} in units of mL/min/kg) was then calculated from in vitro $t_{1/2}$ data using the following parameters: hepatocytes per gram liver (million cells/g; mouse=135, rat = 120, dog = 240, minipig = 124, human = 120) and liver weight per kg of body weight (g/kg; mouse = 87.5, rat = 40, dog = 32, minipig = 16, human = 25.7).

LC-MS/MS

CADD522 was quantified using LC-MS/MS (SCIEX API 4000, negative ESI) with tizoxanide (Merck, SML2837) as internal standard. The assay was linear (6–766 nmol/L; r^2>0.98), with intra- and inter-assay CVs ≤15% and recovery of 74–104%.

Cell culture

PHMLEB (RRID: CVCL_DG84; human breast epithelium) stably expressing *TWIST2* named TWIST2+ cells were kindly provided by Michele Vitolo and Stuart Martin at the University of Maryland Greenebaum Cancer Center. MCF7 (RRID: CVCL_0031; human ER+ breast cancer) were obtained from the American Type Culture Collection. Cells were authenticated by STR profiling[45]. PHMLEB and TWIST2+ cells were cultured in MEBM (Lonza, 11695430) supplemented with SingleQuots Supplement CC-4136 (Lonza, CC-3150). MCF7 were cultured in DMEM (Lonza, BE15-604K) supplemented with 10% FBS and 1% (v/v) penicillin/streptomycin. Cells were maintained at 37 °C in 5% CO_2. Experiments were performed with *Mycoplasma* free cells. Adherent tissue culture plates were precoated with FNC Coating Mix (AthenaES, ACT1-0407-100). Ultra-low attachment plates (Corning, 3261) and EBM-2 (Lonza, CC-3162) were used for the suspension cultures.

CETSA

RUNX2 engagement in MDA-MB-231 cells (RRID: CVCL_0062; human triple-negative breast cancer) was tested using CETSA[46,47] applying a 38–60 °C gradient with/without CADD522 (0.64-10,000 nM) for 10 min. After centrifugation at 14,000 × *g* to remove denatured protein, supernatant was collected and resolved via SDS-PAGE followed by immunoblot analysis with RUNX2 antibody (Cell Signaling Technologies, 8486S). Bands were quantified with a C-DiGit Blot Scanner (LI-COR Biosciences) and subsequent $T_{agg}(50)$ and $T_{agg}(75)$ values, described as temperatures at which 50/75% of the initial protein was reduced, respectively, were calculated.

In vitro assays

Clonogenic growth of MCF7 cells was assessed by CFA after CADD522 or analogue treatment (20, 100 μM) over 21 days. Colonies were fixed in 3:1 methanol-acetic acid solution, stained with 0.5% crystal violet and washed with PBS. Spheroid growth of PHMLEB and TWIST2+ cells (~100,000 cells/well) was measured after CADD522 (0, 10, 50 μM) over 14 days. Spheroids were photographed and measured from 4 fields per well and averaged from duplicate wells.

Statistical analyses

Data were analysed using Prism v7 (GraphPad), SPSS v28 (IBM) and Stata v14 (StataCorp). Data distributions were assessed for normality using the Shapiro-Wilk test prior to parametric analyses. Comparisons among three or more independent groups were performed using one-way analysis of variance (ANOVA) followed by Tukey's multiple comparisons test. Comparisons between two independent groups were performed using two-tailed unpaired t-tests, with Welch's correction applied where variances were unequal. Paired t-tests were used for matched observations. Results are presented as mean ± SEM or SD, as indicated. A two-sided $p < 0.05$ was considered statistically significant ($^{*}p \le 0.05$, $^{**}p \le 0.01$, $^{***}p \le 0.005$, $^{****}p \le 0.001$).

Data availability

All data generated or analysed during this study are included in this published article and its Supplementary Information. Additional datasets and detailed methodological protocols required to support reproducibility are available from the corresponding author upon reasonable request.

Received: 8 January 2025; Accepted: 14 August 2026;
Published online: 07 September 2026

References

1. Eastell, R. et al. Postmenopausal osteoporosis. *Nat. Rev. Dis. Prim.* **2**, 16069. https://doi.org/10.1038/nrdp.2016.69 (2016).
2. Hassan, N. et al. Rare and common variants in GALNT3 may affect bone mass independently of phosphate metabolism. *J. Bone Miner. Res. Off. J. Am. Soc. Bone Miner. Res.* **38**, 678–691, https://doi.org/10.1002/jbmr.4795 (2023).
3. Lee, Y. K., Lee, Y. J., Ha, Y. C. & Koo, K. H. Five-year relative survival of patients with osteoporotic hip fracture. *J. Clin. Endocrinol. Metab.* **99**, 97–100, https://doi.org/10.1210/jc.2013-2352 (2014).
4. Burge, R. et al. Incidence and economic burden of osteoporosis-related fractures in the United States, 2005-2025. *J. Bone Miner. Res. Off. J. Am. Soc. Bone Miner. Res.* **22**, 465–475, https://doi.org/10.1359/jbmr.061113 (2007).
5. Kanis, J. A., Delmas, P., Burckhardt, P., Cooper, C. & Torgerson, D. Guidelines for diagnosis and management of osteoporosis. *Eur. Found. Osteoporos. Bone Dis. Osteoporos. Int. J. Established Result Cooperation Eur. Found. Osteoporos. Natl. Osteoporos. Found. USA* **7**, 390–406, https://doi.org/10.1007/bf01623782 (1997).
6. Chen, J. F., Lin, P. W., Tsai, Y. R., Yang, Y. C. & Kang, H. Y. Androgens and androgen receptor actions on bone health and disease: from androgen deficiency to androgen therapy. *Cells* **8** https://doi.org/10.3390/cells8111318 (2019).
7. Tang, J. C. Y. et al. LC-MS/MS application for urine free pyridinoline and free deoxypyridinoline: Urine markers of collagen and bone degradation. *Clin. Mass Spectrom.* **1**, 11–18, https://doi.org/10.1016/j.clinms.2016.08.001 (2016).
8. Singh, M. & Gonegandla, G. S. Bisphosphonate-induced osteonecrosis of the jaws (BIONJ). *J. Maxillofac. oral. Surg.* **19**, 162–167, https://doi.org/10.1007/s12663-019-01211-2 (2020).
9. Koller, G. et al. Persistence and adherence to parenteral osteoporosis therapies: a systematic review. *Osteoporos. Int. J. Established Result Cooperation Eur. Found. Osteoporos. Natl. Osteoporos. Found. USA* **31**, 2093–2102, https://doi.org/10.1007/s00198-020-05507-9 (2020).
10. McClung, M. R. et al. Romosozumab in postmenopausal women with low bone mineral density. *N. Engl. J. Med.* **370**, 412–420, https://doi.org/10.1056/NEJMoa1305224 (2014).
11. Manson, J. E. et al. Menopausal hormone therapy and health outcomes during the intervention and extended poststopping phases of the Women's Health Initiative randomized trials. *JAMA J. Am. Med. Assoc.* **310**, 1353–1368, https://doi.org/10.1001/jama.2013.278040 (2013).
12. Lufkin, E. G. et al. Treatment of postmenopausal osteoporosis with transdermal estrogen. *Ann. Intern. Med.* **117**, 1–9, https://doi.org/10.7326/0003-4819-117-1-1 (1992).
13. Stevenson, J. Prevention and treatment of osteoporosis in women. *Post Reprod. Health* **29**, 11–14, https://doi.org/10.1177/20533691221139902 (2023).
14. Green, D. et al. YBX1-interacting small RNAs and RUNX2 can be blocked in primary bone cancer using CADD522. *J. Bone Oncol.* **39**, 100474. https://doi.org/10.1016/j.jbo.2023.100474 (2023).
15. Kim, M. S., Gernapudi, R., Choi, E. Y., Lapidus, R. G. & Passaniti, A. Characterization of CADD522, a small molecule that inhibits RUNX2-DNA binding and exhibits antitumor activity. *Oncotarget* **8**, 70916–70940, https://doi.org/10.18632/oncotarget.20200 (2017).
16. Kim, M. S. et al. Targeting breast cancer metabolism with a novel inhibitor of mitochondrial ATP synthesis. *Oncotarget* **11**, 3863–3885, https://doi.org/10.18632/oncotarget.27743 (2020).
17. Mendes, E. A. et al. RUNX2 inhibition disrupts a PAX3::FOXO1-RUNX2 feed-forward loop and dismantles oncogenic gene programs in fusion-positive rhabdomyosarcoma. *bioRxiv Prepr. Serv. Biol.* https://doi.org/10.1101/2025.07.21.665972 (2025).
18. Green, D., Dalmay, T. & Fraser, W. D. Role of miR-140 in embryonic bone development and cancer. *Clin. Sci.* **129**, 863–873, https://doi.org/10.1042/cs20150230 (2015).
19. Green, D. et al. Biological sample collection to advance research and treatment: a Fight Osteosarcoma Through European Research (FOSTER) and Euro Ewing Consortium (EEC) statement. *Clin. Cancer Res. Off. J. Am. Assoc. Cancer Res.* https://doi.org/10.1158/1078-0432.ccr-24-0101 (2024).

20. Gupta, S. et al. RUNX2 (6p21.1) amplification in osteosarcoma. *Hum. Pathol.* **94**, 23–28, https://doi.org/10.1016/j.humpath.2019.09.010 (2019).
21. Kim, Y. I. et al. SOX9 is a key component of RUNX2-regulated transcriptional circuitry in osteosarcoma. *Cell Biosci.* **13**, 136, https://doi.org/10.1186/s13578-023-01088-2 (2023).
22. Liu, S. F. et al. RUNX2 is stabilised by TAZ and drives pulmonary artery calcification and lung vascular remodelling in pulmonary hypertension due to left heart disease. *Eur. Respir. J.* **64** (2024). https://doi.org/10.1183/13993003.00844-2023
23. Komori, T. Runx2, a multifunctional transcription factor in skeletal development. *J. Cell. Biochem.* **87**, 1-8 (2002). https://doi.org/10.1002/jcb.10276
24. Kundu, M. et al. Cbfbeta interacts with Runx2 and has a critical role in bone development. *Nat. Genet.* **32**, 639–644, https://doi.org/10.1038/ng1050 (2002).
25. Ito, Y. & Miyazono, K. RUNX transcription factors as key targets of TGF-beta superfamily signaling. *Curr. Opin. Genet. Dev.* **13**, 43–47 (2003).
26. Fujita, T. et al. Runx2 induces osteoblast and chondrocyte differentiation and enhances their migration by coupling with PI3K-Akt signaling. *J. Cell Biol.* **166**, 85–95, https://doi.org/10.1083/jcb.200401138 (2004).
27. Schroeder, T. M., Jensen, E. D. & Westendorf, J. J. Runx2: a master organizer of gene transcription in developing and maturing osteoblasts. *Birth Defects Res C. Embryo Today* **75**, 213–225, https://doi.org/10.1002/bdrc.20043 (2005).
28. Chen, H. et al. Runx2 regulates endochondral ossification through control of chondrocyte proliferation and differentiation. *J. Bone Miner. Res. Off. J. Am. Soc. Bone Miner. Res.* **29**, 2653–2665, https://doi.org/10.1002/jbmr.2287 (2014).
29. Komori, T. Whole aspect of Runx2 functions in skeletal development. *Int. J. Mol. Sci.* **23** https://doi.org/10.3390/ijms23105776 (2022).
30. Bull, E. C. et al. Targeting metastasis in paediatric bone sarcomas. *Mol. Cancer* **24**, 153. https://doi.org/10.1186/s12943-025-02365-z (2025).
31. Green, D. et al. Targeting the MAPK7/MMP9 axis for metastasis in primary bone cancer. *Oncogene* **39**, 5553–5569, https://doi.org/10.1038/s41388-020-1379-0 (2020).
32. Pontifex, M. G. et al. APOE4 genotype exacerbates the impact of menopause on cognition and synaptic plasticity in APOE-TR mice. *FASEB J. Off. Publ. Federation Am. Societies Exp. Biol.* **35**, e21583. https://doi.org/10.1096/fj.202002621RR (2021).
33. Pontifex, M. G. et al. DHA-enriched fish oil ameliorates deficits in cognition associated with menopause and the APOE4 genotype in rodents. *Nutrients* **14** https://doi.org/10.3390/nu14091698 (2022).
34. Alexandrov, A. I., Mileni, M., Chien, E. Y., Hanson, M. A. & Stevens, R. C. Microscale fluorescent thermal stability assay for membrane proteins. *Struct. (Lond., Engl. : 1993)* **16**, 351–359, https://doi.org/10.1016/j.str.2008.02.004 (2008).
35. Crichton, P. G. et al. Trends in thermostability provide information on the nature of substrate, inhibitor, and lipid interactions with mitochondrial carriers. *J. Biol. Chem.* **290**, 8206–8217, https://doi.org/10.1074/jbc.M114.616607 (2015).
36. Lee, Y., Willers, C., Kunji, E. R. & Crichton, P. G. Uncoupling protein 1 binds one nucleotide per monomer and is stabilized by tightly bound cardiolipin. *Proc. Natl. Acad. Sci. USA* **112**, 6973–6978, https://doi.org/10.1073/pnas.1503833112 (2015).
37. Echtay, K. S., Bienengraeber, M. & Klingenberg, M. Mutagenesis of the uncoupling protein of brown adipose tissue. Neutralization Of E190 largely abolishes pH control of nucleotide binding. *Biochemistry* **36**, 8253–8260, https://doi.org/10.1021/bi970513r (1997).
38. Garlid, K. D., Orosz, D. E., Modriansky, M., Vassanelli, S. & Jezek, P. On the mechanism of fatty acid-induced proton transport by mitochondrial uncoupling protein. *J. Biol. Chem.* **271**, 2615–2620, https://doi.org/10.1074/jbc.271.5.2615 (1996).
39. Orosz, D. E. & Garlid, K. D. A sensitive new fluorescence assay for measuring proton transport across liposomal membranes. *Anal. Biochem.* **210**, 7–15, https://doi.org/10.1006/abio.1993.1143 (1993).
40. Cavalieri, R. et al. Activating ligands of Uncoupling protein 1 identified by rapid membrane protein thermostability shift analysis. *Mol. Metab.* **62**, 101526. https://doi.org/10.1016/j.molmet.2022.101526 (2022).
41. Martinsen, A. et al. Altered SPMs and age-associated decrease in brain DHA in APOE4 female mice. *FASEB J. Off. Publ. Federation Am. Societies Exp. Biol.* **33**, 10315–10326, https://doi.org/10.1096/fj.201900423R (2019).
42. Christie, W. W. Gas chromatography-mass spectrometry methods for structural analysis of fatty acids. *Lipids* **33**, 343–353, https://doi.org/10.1007/s11745-998-0214-x (1998).
43. Byrne, C. J., Fair, S., Dick, J. R., Lonergan, P. & Kenny, D. A. Dietary supplementation with fish oil and safflower oil, during the finishing period, alters brisket muscle fatty acid profile and n-6/n-3 ratio but not carcass traits of dairy beef bulls. *Appl. Anim. Sci.* **37**, 436–444, https://doi.org/10.15232/aas.2021-02158 (2021).
44. Zang, T. et al. Simultaneous quantitation of nine hydroxy-androgens and their conjugates in human serum by stable isotope dilution liquid chromatography electrospray ionization tandem mass spectrometry. *J. Steroid Biochem. Mol. Biol.* **165**, 342–355, https://doi.org/10.1016/j.jsbmb.2016.08.001 (2017).
45. Almeida, J. L. & Korch, C. T. in Assay Guidance Manual (eds S. Markossian et al.). Eli Lilly & Company and the National Center for Advancing Translational Sciences, (2004).
46. Jafari, R. et al. The cellular thermal shift assay for evaluating drug target interactions in cells. *Nat. Protoc.* **9**, 2100–2122, https://doi.org/10.1038/nprot.2014.138 (2014).
47. Her, N. G., Babic, I., Yenugonda, V. M., Kesari, S. & Nurmemmedov, E. Cellular thermal shift analysis for interrogation of CRISPR-assisted proteomic changes. *BioTechniques* **68**, 180–184, https://doi.org/10.2144/btn-2019-0100 (2020).

Acknowledgements

This work was supported by The Sir William Coxen Trust Fund (D.G.), a VA Merit Review Award from the US Department of Veterans Affairs Biomedical Laboratory Research and Development Service (I01-BX002205A, A.P.) and the Cigarette Restitution Fund of the State of Maryland at the University of Maryland Greenebaum Comprehensive Cancer Center (A.P.). We thank Michele Vitolo and Stuart Martin at the University of Maryland for PHMLEB and TWIST2+ cells, and the Translational Laboratory Shared Resources (TLSR) staff for technical support. We also thank Daniel Gustafson, Peter Gaskin, Sarah Gould, Ian Fraser and Darren Matthews for their DMPK expertise; and David Ellis, Emma Johnson, Samuel Lawrence and Joita Dey for their business support. We are especially grateful to Michael Mainelli for his continued and invaluable advice. Finally, we wish to dedicate this work to Prof. William D. Fraser who sadly passed away while working on this project. For open access purposes, the corresponding author has applied a CC BY public copyright licence to any Author Accepted Manuscript.

Author contributions

A.E., M.S.K., C.S., I.P., A.M., E.N., E.C.B., T.B., R.D., J.R.D., R.L., D.M.C., and M.G.P. performed experiments. J.C.Y.T., P.G.C., M.G.P., W.D.F., N.J.H., A.P. and D.G. developed protocols and provided resources. A.E., M.S.K., P.G.C., M.G.P., W.D.F., N.J.H., A.P. and D.G. curated research data and performed formal data analysis. W.D.F., N.J.H., A.P. and D.G. supervised the study. W.D.F., A.P. and D.G. conceptualised the study and obtained funding. D.G. wrote the paper. All authors reviewed and approved the final manuscript.

Competing interests

W.D.F. and D.G. report patents EP3897609B1, WO2023209077A1, and patents pending PCT/EP2023/061092 and WO2023/209077. A.P. reports patents US10329246B2 and US11634381B2. All other authors declare no competing interests.

Additional information

Supplementary information The online version contains supplementary material available at https://doi.org/10.1038/s44386-026-00076-z.

Correspondence and requests for materials should be addressed to Antonino Passaniti or Darrell Green.